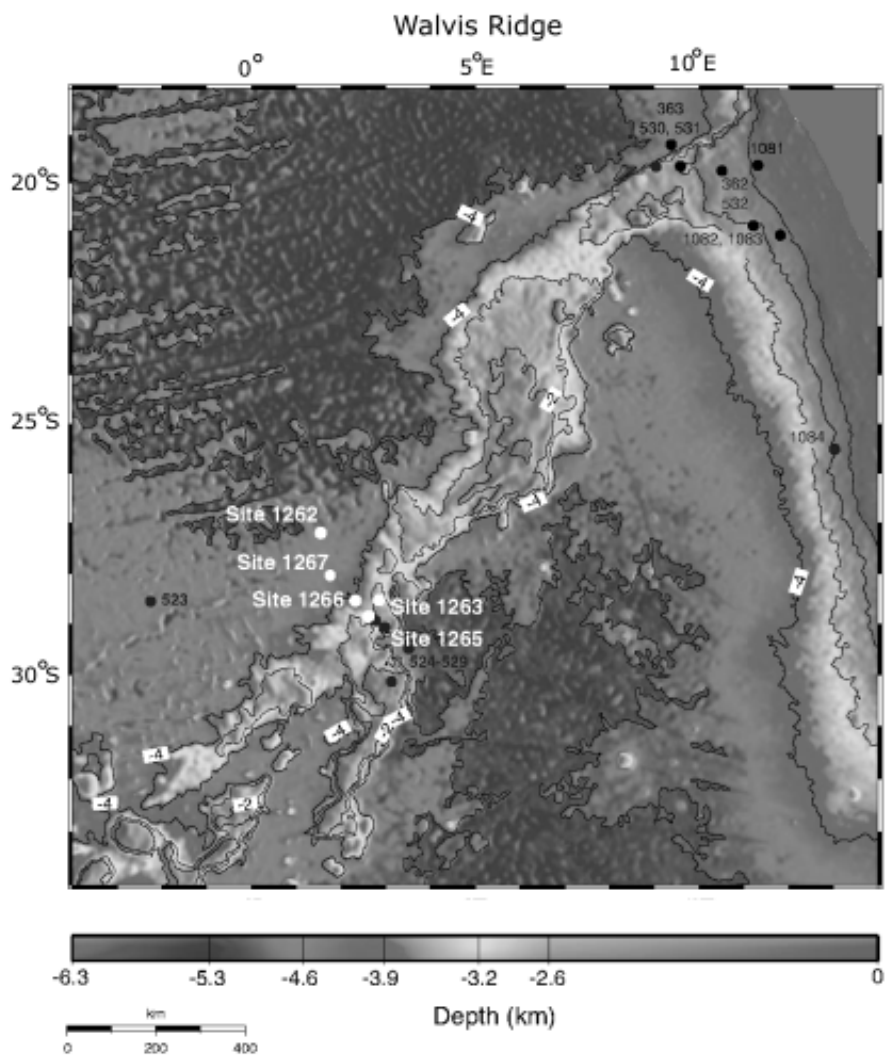Supporting Chapter 1 of this thesis, this appendix contains two figures and two tables, additional references, and extended description of methods used and discussion on calcareous nannofossil biostratigraphy.

Appendix Figure 2.1 Location map of the Walvis Ridge Sites recovered during ODP Leg 208 (Zachos et al., 2004) and DSDP Legs 73 and 74 (Moore et al., 1984).

Methods

Bulk samples (2-3 mg) were collected from the surfaces of split cores during the cruise. The samples were freeze-dried and ground. Stable isotope analyses were conducted on automated gas source mass spectrometers in four laboratories. The Site 1262 and 1266 records were generated on an Autocarb prep system coupled to a PRISM Mass Spectrometer (MS) at the University of California, Santa Cruz. The Site 1263 record was generated on a Kiel device coupled to MAT 252 MS at Amsterdam University. The Site 1267 record was generated on an Isocarb coupled to a PRISM MS at the University of Florida, and the Site 1265 record was generated on a Kiel device coupled to a MAT 251 MS at Bremen University. Analytical precision based on replicate analyses of standards was better than $\pm 0.05‰$ for $\delta^{13}C$. All values are reported relative to vPDB.

Biostratigraphy

Biohorizons N1 to N4 are delineated from the abundance patterns of the following selected taxa: the genus *Fasciculithus* (*Fasciculithus* spp.), *Rhomboaster calcitrapa* group (as defined by Raffi et al., 2005), *Zygrhablithus bijugatus*. "Base" and "Top" indicates the first and last occurrence of the taxon (Appendix Table 2.1).

N1 - Decrease in diversification of *Fasciculithus* spp. The uppermost Paleocene diversified fasciculith assemblage includes different species, as *F. thomasii*, *F. alanii*, rare *F. richardii* and *F. schaubii*, and abundant *F. tympaniformis* and *F. involutus*. At the onset of CIE fasciculiths show a drastic decrease in diversity and abundance compared to the pre-boundary situation. The two remaining species *(F. involutus* and *F. tympaniformis)* are consistently present (show peaks in abundance) throughout the CIE. This event is recorded in the known Paleocene-Eocene (P/E) boundary sections, from different areas at different latitudes (Backman, 1986; Monechi et al., 2000).

N2 - Base of *Rhomboaster calcitrapa* gr. Within the CIE, *Rhomboaster* morphotypes belonging to the spined *R. calcitrapa* group and *R. cuspis* have the lowermost occurrence. *R. calcitrapa* gr. specimens have been consistently observed in most of the known P/E boundary sections (Cramer et al., 1999; Monechi et al., 2000; Aubry, 2001; Kahn and Aubry, 2004), and appears to represent a globally distributed evolutionary event (Raffi et al., 2005).

N3 - Relative increase *Zygrhablithus bijugatus*/ decrease *Fasciculithus* (the "*Fasciculithus* spp./ *Zygrhablithus bijugatus* abundance cross-over"). The demise of fasciculiths occurs concomitantly with the initial rise (Site 1263) or marked abundance increase (Site 1262) of *Zygrhablithus bijugatus*. In sedimentary successions from the North and South Atlantic oceans, the Indian Ocean, the Shatsky Rise in subtropical

Pacific Ocean, and from Tethyan area, this cross-over in abundance was consistently observed close to the P/E boundary (Bralower, 2002; Tremolada and Bralower, 2004; Gibbs et al., 2006) whereas *Z. bijugatus* is very rare or missing, implying that this particular early Eocene turnover is absent in equatorial regions (Raffi et al., 2005).

N4 - Top of *Rhomboaster calcitrapa* gr. The characteristic presence of spined *Rhomboaster* spp. is restricted to the CIE interval at Sites 1263 and 1262. Similar distribution range has been recorded in several P/E sections, from different areas at different latitudes (Cramer et al., 1999; Monechi et al., 2000; Aubry, 2001; Kahn and Aubry, 2004).

Appendix Table 2.1 Calcareous nannofossil biohorizons

biohorizon		1263 (mcd)	1263 samples	1262 (mcd)	1262 samples
N4	Top R.calcitrapa gr.	334.52	1263C-14H-2,31-32	139.71	1262B-15H-3,28-29
		334.7	1263C-14H-2,49-50	139.72	1262B-15H-3,29-30
N4a	decrease R.calcitrapa gr.	334.71	1263C-14H-2,50-51	139.76	1262B-15H-3,33-34
		334.72	1263C-14H-2,51-52	139.77	1262B-15H-3,34-35
N3	X fasciuliths/Z.bijugatus	334.77	1263C-14H-2,56-57	139.77	1262B-15H-3,34-35
	(decrease fasciculiths)	334.8	1263C-14H-2,59-60	139.79	1262B-15H-3,36-37
N3a	beginning decrease in abundance of fasciculiths	334.9	1263C-14H-2,70-71	139.83	1262B-15H-3,50-51
N2	Base R.calcitrapa gr.	335.25	1263C-14H-2,104-105	140.01	1262B-15H-3,58-59
		335.26	1263C-14H-2,105-106	140.02	1262B-15H-3,59-60
N1a	2nd Decrease in diversity of fasciculiths	335.26	1263C-14H-2,107-108	barren	interval
		335.28	1263C-14H-2,108-109		
N1	1st Decrease in diversity of fasciculiths	335.6	1263D-4H-1,67-68	140.145	1262B-15H-3,73
		335.61	1263D-4H-1,68-69	140.15	1262B-15H-3,72-74

157

Appendix Table 2.2 Carbon isotope tie points from ODP Site 690 and assigned ages used for correlation and dating the Leg 208 P-E boundary sections. Depths are in meters composited depth (MCD). * Time (kyr) at ODP Site 690 relative to the P-E boundary set to 55 Ma. Ages are from Röhl et al. (2000), and Farley and Eltgroth (2003). For tie points G&H, because of the large differences in the two age models, we used the means for the 2080 age model. ** Magnetic susceptibility (MS) tie points are from Zachos et al. (2004). *** For Sites 1262, 1266 and 1267, the depths of tie points C&B were estimated by lenear interpolation between points D&A using the temporal relationship established at Site 1263.

| Tie Points	690 mbsf	690 Age (±kyr) Roehl00)*	690 Age (±kyr) F&E03)*	1262A (Mcd)	1263B, C, D (Mcd)	1265 (Mcd)	1266 (Mcd)	1267A (Mcd)	1267B (Mcd)
MS tie point**	166.13	230	183	138.08	331.19	312.64	303.84	229.40	227.35
H	167.12	218	118.6	139.20	333.14	314.50	305.37	230.50	230.46
G	169.05	108	100.15	139.40	333.73	314.70	305.60	230.75	230.66
F	169.39	88	93.6	139.73	334.56	315.39	306.13	231.15	231.15
E	169.56	76	90.2	139.83	334.75	315.56	306.44	231.29	231.29
D	170.02	47.2	67	139.92	335.10	315.70	306.56	231.46	231.41
C***	170.33	28.4	37.48	139.99	335.22	315.75	306.64	231.48	231.46
B***	170.33	1	1	140.04	335.39	315.88	306.69	231.52	231.49
A	170.63	1		140.11	335.68	315.88	306.77	231.56	231.54
PEB	170.64	0	0	140.12	335.69	315.89	306.78	231.57	231.55
A-	171.24	-34	-62	140.15	336.00	316.05	306.97	231.73	231.68
B-	171.24	-125		141.15	337.82	317.69	308.43	232.82	231.98
MS tie point**	172.81			142.58	340.42		310.51	234.38	236.28

Appendix 3

Supporting Chapter 2 of this thesis, this appendix contains six figures, additional references, and extended description of methods used and discussion on magnetobiostratigraphy, magnetic susceptibility (MS) and $CaCO_3$ weight % scales shown in Figure 1, spectral results, astronomical phase relations and global significance of the ETM2 event (and *Elmo* horizon).
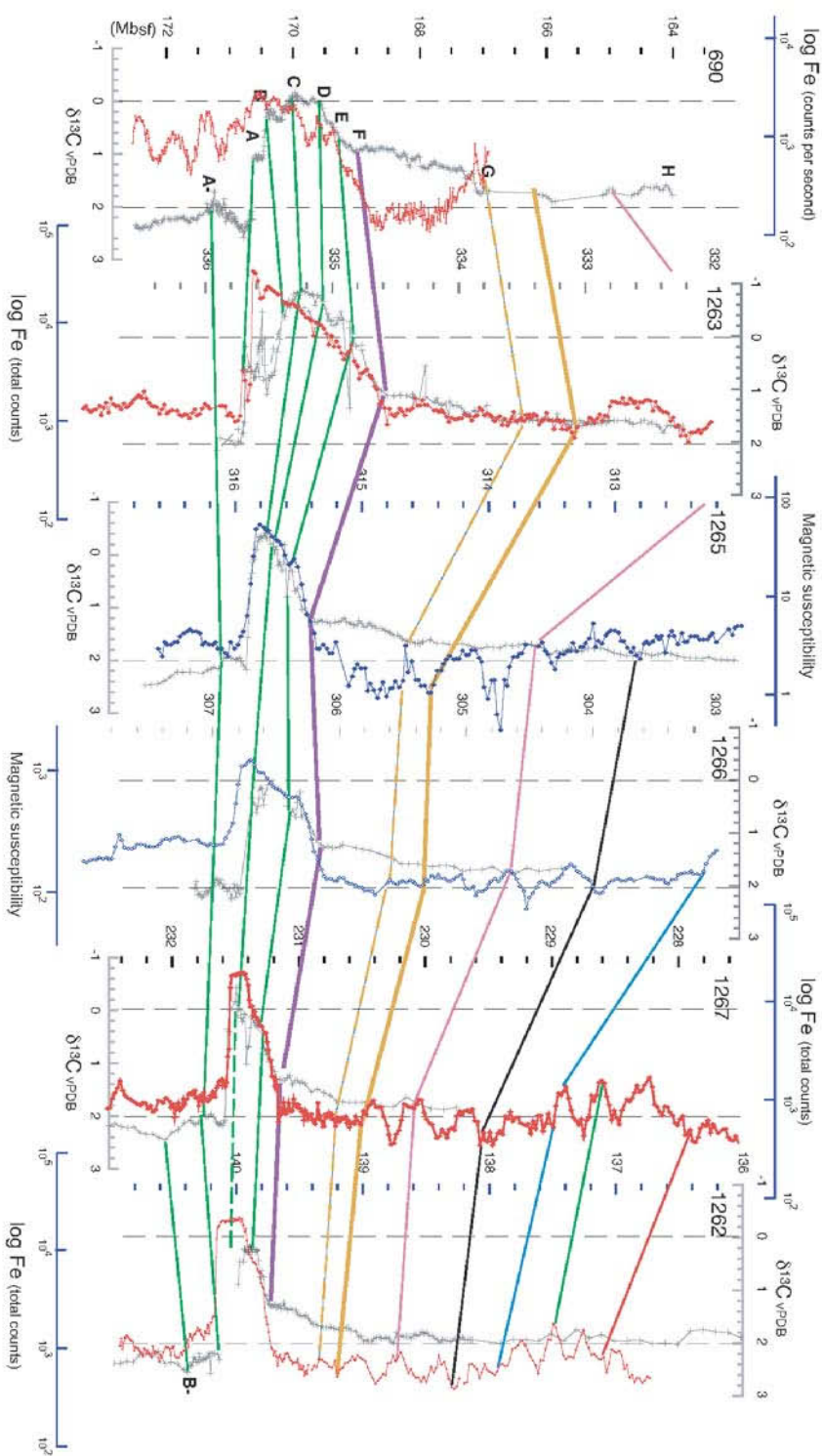
Appendix Figure 2.2 High resolution Fe concentration records or MS records for ODP Sites 1262, 1263, 1265, 1266, and 1266. Fe concentration was determined using an XRF core scanner at Bremen University Core Repository.
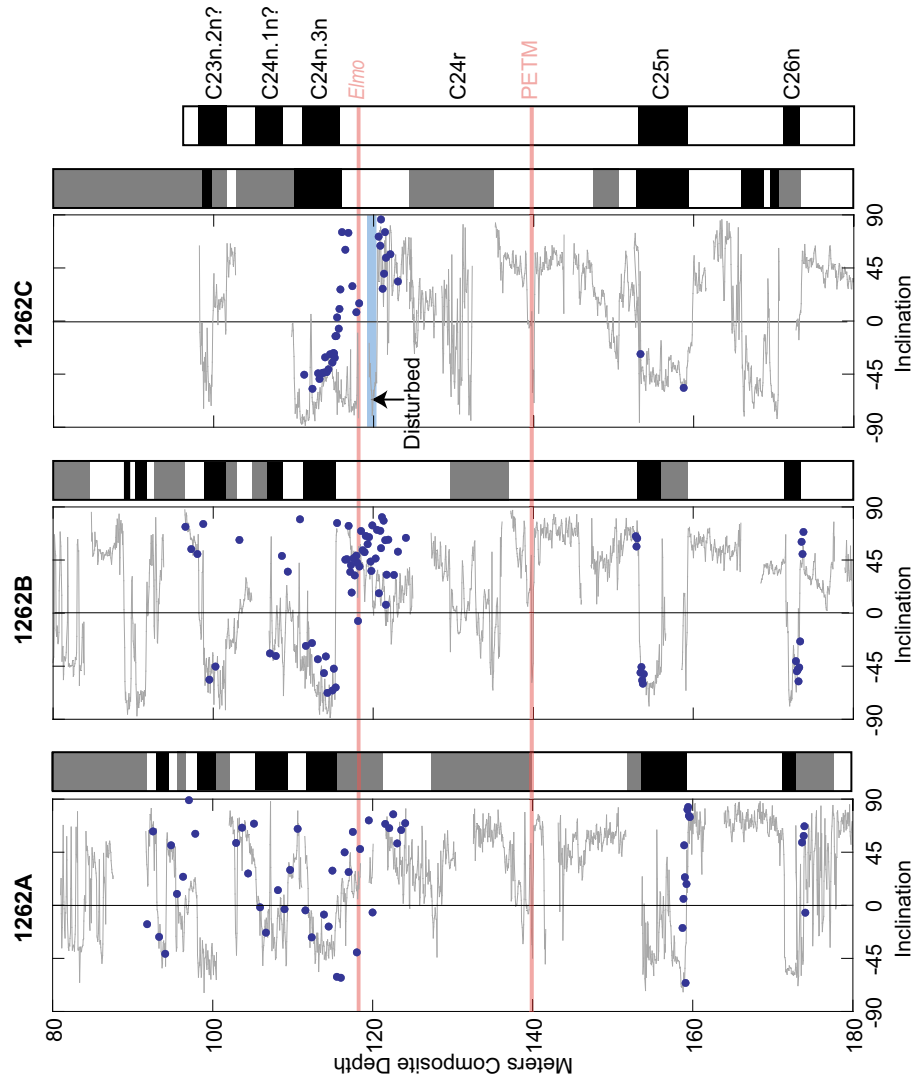
Appendix Figure 3.1 Late Palaeocene to early Eocene magnetostratigraphy for ODP Site 1262. Shipboard pass-through inclination (demagnetized to 15 mT; grey lines) and discrete sample inclination (principle component calculated from 20 to 40 mT; blue circles). Shaded interval on site 1262C represents a particularly disturbed core section, results from which should not be considered reliable. Overall magnetostratigraphic interpretation to right. Black = normal polarity; white = reverse; grey = indeterminate.
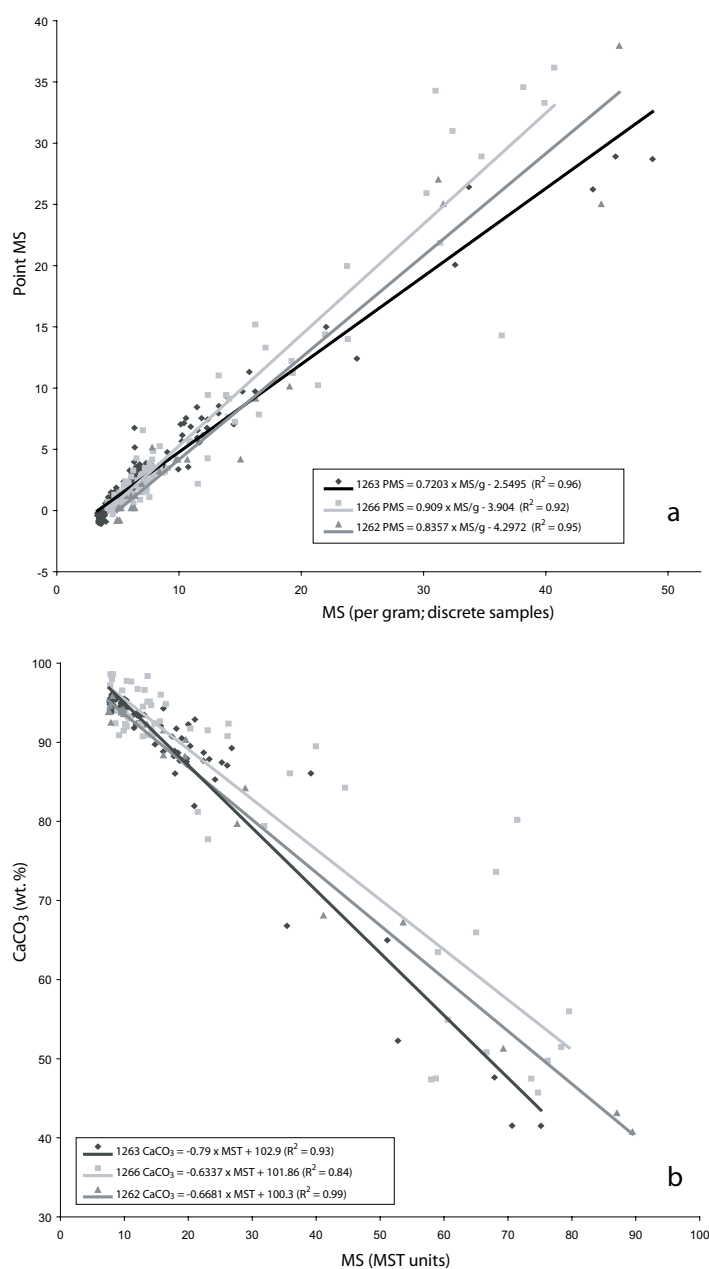
Appendix Figure 3.2 Regression analyses for the magnetic susceptibility to calcium carbonate weight percentage conversion of Sites 1262, 1263 and 1267. a, Magnetic susceptibility per gram sediment (MS/g) versus shipboard point magnetic susceptibility (PMS). The MS/g values were converted to the shipboard magnetic susceptibility scale of the multi sensor track (MS-MST) using the displayed function for each site and the equation MS-MST = PMS x 2.0683 + 7.8257 (R2 = 0.99) (Zachos et al., 2004). b, MS/g (on the recalibrated MS-MST scale) versus CaCO3 weight%.
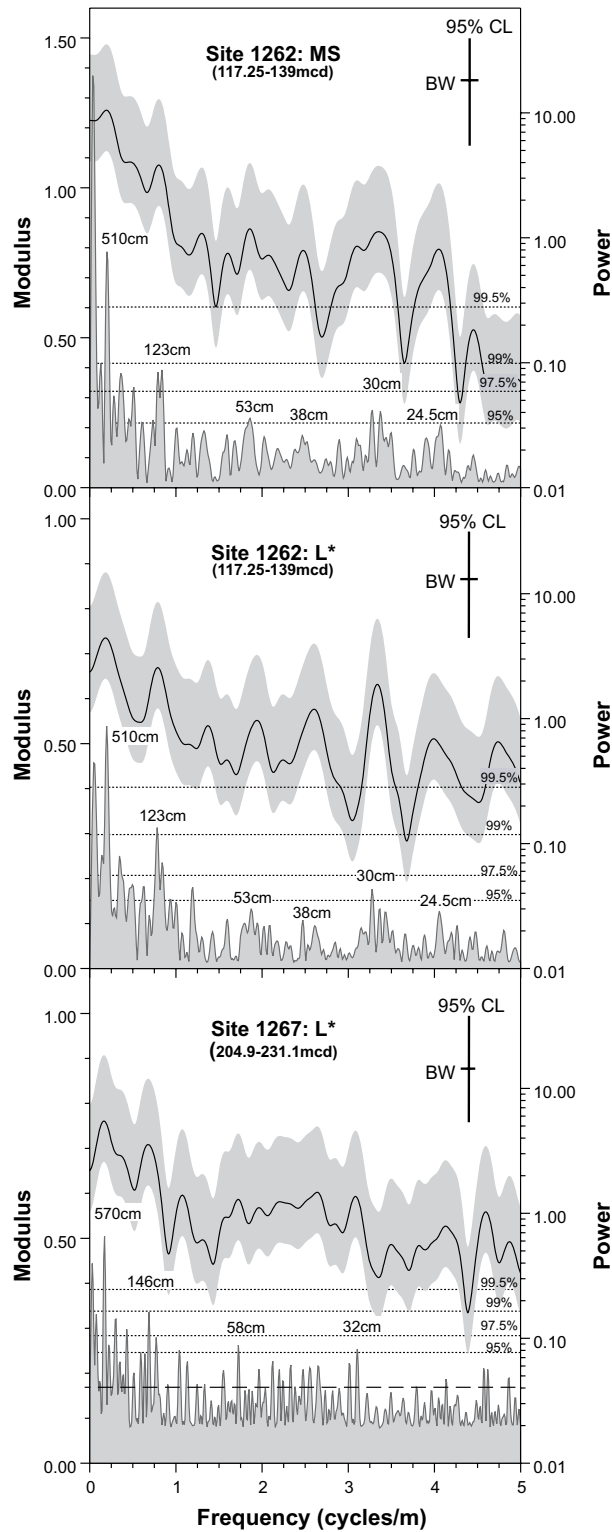
Appendix Figure 3.3 Frequency spectra of the magnetic susceptibility and color reflectance records of Sites 1262 and 1267 for the Elmo-PETM interval. Results of the CLEAN-algorithm and Blackman-Tukey (BT) are expressed by their modulus and power, respectively. Horizontal dotted lines indicate the 95, 97.5, 99, and 99.5% significance level of the CLEANED-spectra. Bandwidth (BW) and 95% confidence limits (CF) of the BT spectra are based on a Tukey window with a number of lags that equal 30% the length of the data series.
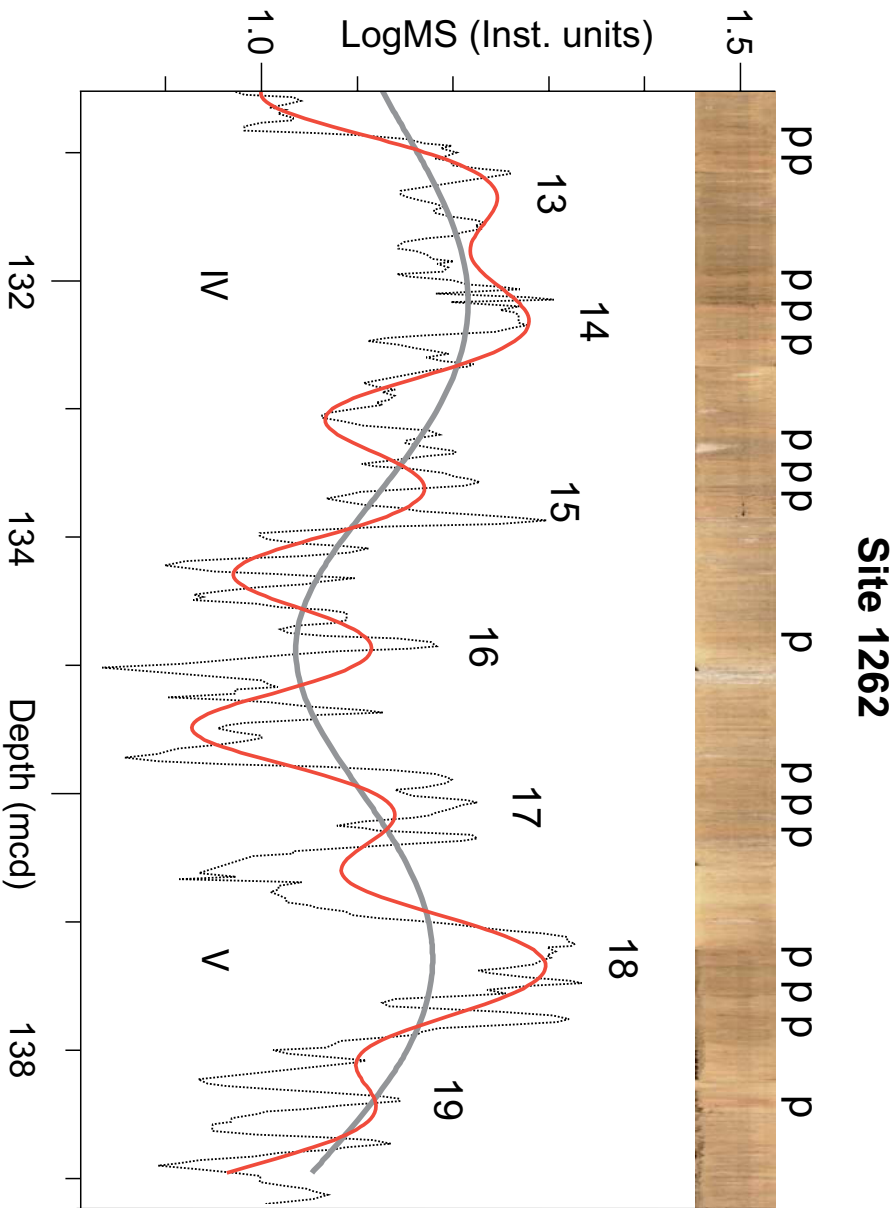
Site 1262

Appendix Figure 3.4 Comparison between precession-related lithological changes and eccentricity cycles in the magnetic susceptibility record of Site 1262. The pink-coloured layers, related to precession, are particularly distinctive during maxima in the short and long-term eccentricity related cycles of the MS record.
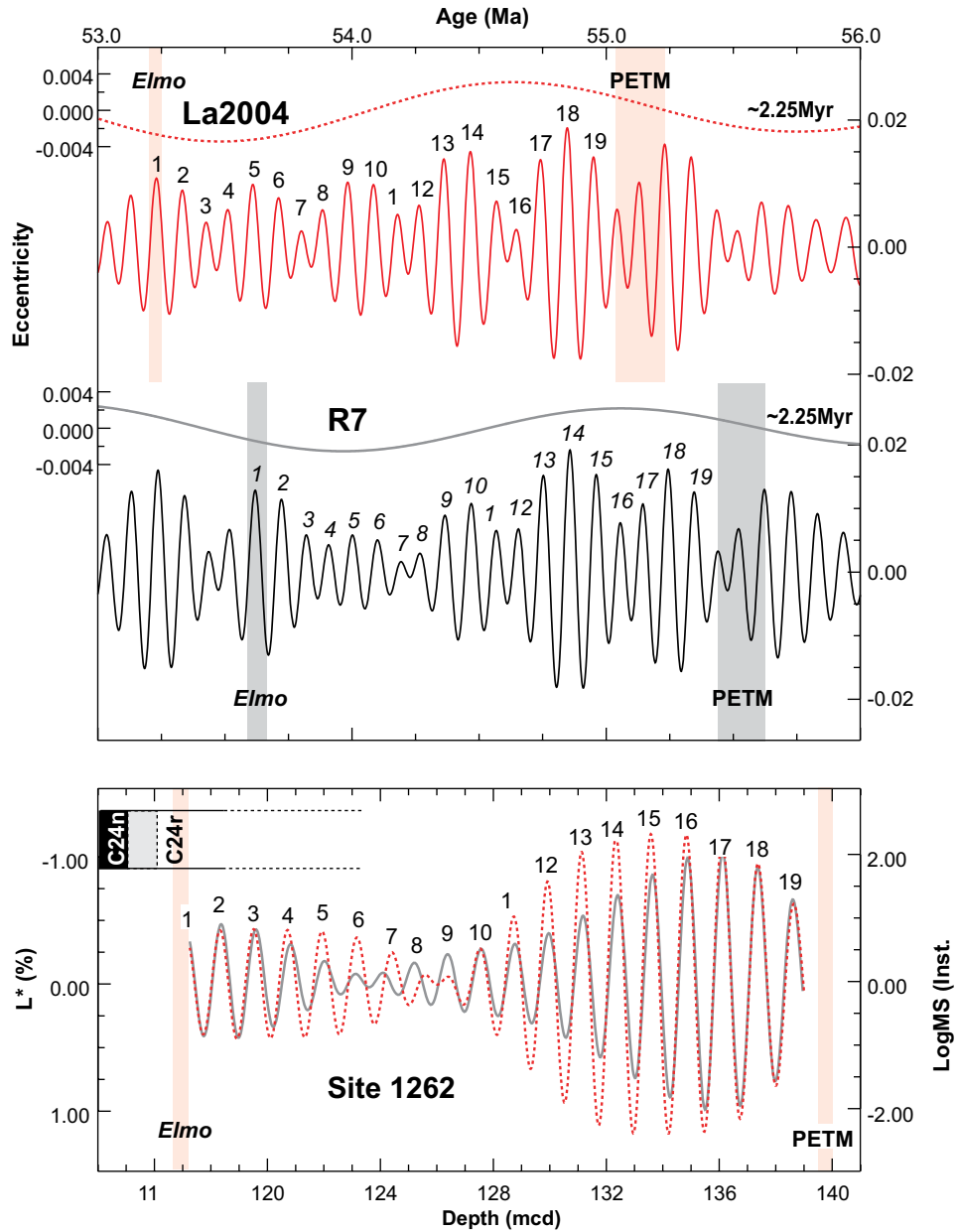
Appendix Figure 3.5 Amplitude modulation of the ~100kyr eccentricity components in Site 1262 and orbital computations. Gaussian filters centred at a frequency of 0.0095 ± 0.002 per kyr and 0.8125 ± 0.1 per meter were applied to extract the ~100kyr eccentricity components from the R7 (Varadi et al., 2003) and La2004 (Laskar et al., 2004) orbital solutions and their correlative cycles from the L* (solid) and MS (dot) records of Site 1262, respectively.

Magnetobiostratigraphy

Discrete samples were taken from the working half cores of Site 1262 in 8 cm^3 cubes. Samples were alternating field (AF) demagnetised in steps up to 60 mT, using the "double-demagnetisation" technique (Tauxe et al., 1995) for AF levels above 30 mT. A drilling overprint was generally removed by 15 mT, and the remanence direction was calculated by principle component analysis (Kirschvink, 1980) for steps from 20 to 40 mT (4 to 6 points). Directions with a maximum angular deviation (Kirschvink, 1980) >10° were rejected. The remaining inclinations were used – along with shipboard pass-through data – to determine polarity.

The new magnetostratigraphic interpretation reveals that the *Elmo* horizon at 117.1-117.2 meters composite depth (mcd) occurs below the C24r/C24n reversal boundary at 115-116mcd (Appendix Fig. 3.1) and not above as it was initially interpreted based on the shipboard measurements (Zachos et al., 2004) alone. The shipboard data are noisy, presumably resulting from a combination of low magnetisation and some drilling and/or splitting related deformation. While the discrete data generally give results consistent with the shipboard results, a notable exception is Hole 1262C, on which the shipboard interpretation was largely based. In this case, the discrete samples—taken from the centre of the cores— are presumed to be less deformed than the whole core, therefore giving more reliable data. In addition, a closer examination of records indicated that the first section in Core 1262C-3H was disturbed (highlighted in Appendix Fig. 3.1), providing unreliable pass-through data. Taken together, discrete and pass-through data from Hole 1262B and the discrete data from Hole 1262C confine the reversal to the interval between 115-116 mcd. The Hole 1262A data show a more gradual transition, but over an interval consistent with that seen in the other holes.

The new magnetostratigraphic interpretation is confirmed by the 20cm-spaced high-resolution calcareous nannofossil biostratigraphy we established for Site 1262. The NP10/NP11 (Martini, 1971) (CP9a/CP9b, Okada and Bukry, 1980) boundary was observed at 118.5 ± 0.1 mcd, where the crossover in abundance between *Tribrachiatus contortus* and *T. orthostylus* is present. Other events which are related to the base of NP11 and maintain the same relative stratigraphic positions are from old to young: top of *Discoaster multiradiatus* at 119.6 ± 0.1 mcd, and the first occurrences of *Spenolithus radians* and *T. orthostylus* at 118.5 ± 0.1 mcd. This shows that NP10/NP11 (CP9a/CP9b) is positioned below the C24r/C24n reversal (and *Elmo* horizon), in accordance with the magnetobiostratigraphic results obtained from previous DSDP holes drilled at Walvis Ridge (Backman, 1986). Furthermore, the lowermost occurrence of *T. orthostylus* was found at 295.75 ± 0.45 mcd in Site 1263, 282.25 ± 0.75 mcd in Site 1265, 295.89 ± 0.45 mcd in Site

1266, 208.35 ± 0.75 mcd in Site 1267, all confirming that the *Elmo* horizon is younger than the NP10/NP11 boundary.

Magnetic susceptibility and CaCO$_3$ weight% scales

The high-resolution MS/g records of Holes 1262A, 1263C, and 1266C were compared to the split core point magnetic susceptibility (PMS) and whole core MS of the multiple sensor track (MS-MST) measurements obtained during Leg 208 (Zachos et al., 2004). We choose to convert all MS data to the MS-MST scale by performing linear regression analyses between MS/g and PMS (Appendix Fig. 3.2a) and the conversion of PMS to MS-MST using the equation MST = PMS x 2.0683 + 7.8257 (R2 = 0.99)(Zachos et al., 2004). Subsequently, a regression analysis between the CaCO$_3$ weight% and the MS/g (converted to the MS-MST scale) of the same samples was applied (Appendix Fig. 3.2b) to obtain the estimated CaCO$_3$ weight% scale of the various sites (Fig. 1).

Spectral results and astronomical tuning procedure

Power spectra were obtained by using the CLEAN transformation (Roberts et al., 1987) and the Blackman-Tukey method (Blackman and Tukey, 1958). For the determination of errors associated with the frequency spectra of the CLEAN algorithm, we applied a Monte Carlo based method (Roberts et al., 1987; Heslop and Dekkers, 2002). Significance levels of 95, 97.5, 99 and 99.5% for the Monte Carlo spectra of the MS and L* depth series were determined by 1) 10% (i.e., Control parameter = 0.1) white noise addition, 2) Clean Gain factor of 0.1, 3) 500 CLEAN Iterations, 4) dt value of 0.02m, and 5) a total number of simulation iterations of 1000. The Blackman-Tukey power spectra were obtained by using the AnalySeries 1.1 software package (Paillard et al., 1996). In this case, data sets were equally spaced and prepared by removing the linear trends. Bandwidths of ~0.19 (Site 1262) and ~0.16 (Site 1267) have been applied as window to smooth the various spectra of the depth series.

The CLEAN (Heslop and Dekkers, 2002) modulus and Blackman-Tukey (Blackman and Tukey, 1958; Paillard et al., 1996) power spectra of L* and MS for Site 1262 revealed consistent and significant peaks at ~510, 123, 53, 38, 30 and 24.5cm (Appendix Fig. 3.3). This frequency distribution of the spectral peaks is in good agreement with that of the astronomical cycles: the periodicities of these cycles equal 96 (short eccentricity), 41.5 (obliquity), 30 (obliquity), 23.5 (precession) and 19.5kyr (precession), respectively, if the ~510cm cycle is a reflection of the 405kyr (long) eccentricity period (Laskar et al., 2004). This assumption is consistent with the shipboard age model, which resulted in an average sedimentation rate for the early Eocene time interval at Site 1262 of ~1.2cm/kyr (Zachos et al., 2004). The correlative depth interval at Site 1267 revealed significant peaks in the L* spectra at ~570, and 146cm, and to a lesser

degree at 58, and 32cm. The long and short eccentricity cycles thus appear to dominate the spectral distribution of this record, whereas the reflection of the obliquity and precession-related cycles is weak and diffuse.

To illustrate how we established the astronomical phase relationship for the extracted short and long eccentricity related MS and L* of Sites 1262 and 1267 (Fig. 2.3), a detail of the lithological changes in the interval just above the PETM of Site 1262 is shown in Appendix Fig. 3.4. This interval clearly reflects the regular occurrence of pink coloured layers (p), which are repeatedly grouped in distinctive bundles of 2-3 layers. The 25-30cm spacing of successive pink coloured layers within one bundle corresponds to the precession-related spectral peaks (Appendix Fig. 3.3), indicating that these layers are precession-forced. Evidently, the bundles are related to the short eccentricity-related MS maxima and are more frequently present during the long eccentricity-related MS maxima. In analogy to the well-known astronomical phase relations for the late Neogene Mediterranean sapropel record (Hilgen, 1991; Hilgen et al., 1995; Lourens et al., 1996), the bundling of pink coloured layers should correspond to a maximum in eccentricity. Due to the eccentricity modulation of the climatic precession cycle, this orbital configuration should have lead to amplified seasonal contrasts on both Hemispheres and hence climate change, thereby triggering the deposition of the pink coloured layers, although it is yet not clear whether these layers should correspond to precession minima or maxima. The near absence of these layers during the long eccentricity-related MS minima further implies that these periods should correspond to minima in the ~405kyr eccentricity cycle, that weakens the effect of the ~100kyr modulation on climatic precession, and hence reduces the precession-driven seasonal contrasts on both Hemispheres.

To investigate whether the very long orbital variations of ~2.25Myr have had an effect on the amplitude changes of the short eccentricity cycles between the PETM and *Elmo* horizon we extracted the ~100kyr component from the L* and MS records of Site 1262 by using a Gaussian filter centred at a frequency of 0.8125 ± 0.1 per meter (Appendix Fig. 3.5). This analysis clearly revealed that the amplitude changes of the ~100kyr cycles are on-average less amplified during the second (II) ~405kyr related cycle of the L* and MS records from Site 1262 (Fig. 3). This spectral characteristic was compared with the minimum amplitude changes in the ~100kyr eccentricity cycles derived from R7 (Varadi et al., 2003)

Appendix Figure 3.6 (right) Global registration of the PETM and Elmo carbon isotope excursions in four well-dated (magneto- and/or nannofossil stratigraphy) sections. **a,** ODP Hole 690B (Southern Ocean; Cramer et al., 2003). **b,** ODP Holes 1051A (red) and 1051B (blue) (Blake Nose, Northwestern Atlantic; Cramer et al., 2003). **c,** Paleosol carbonate isotope record from the Bighorn Basin (Wyoming, USA; Koch et al., 2003). **d,** ODP Site 1262 (this study) and PETM (Chapter 1).
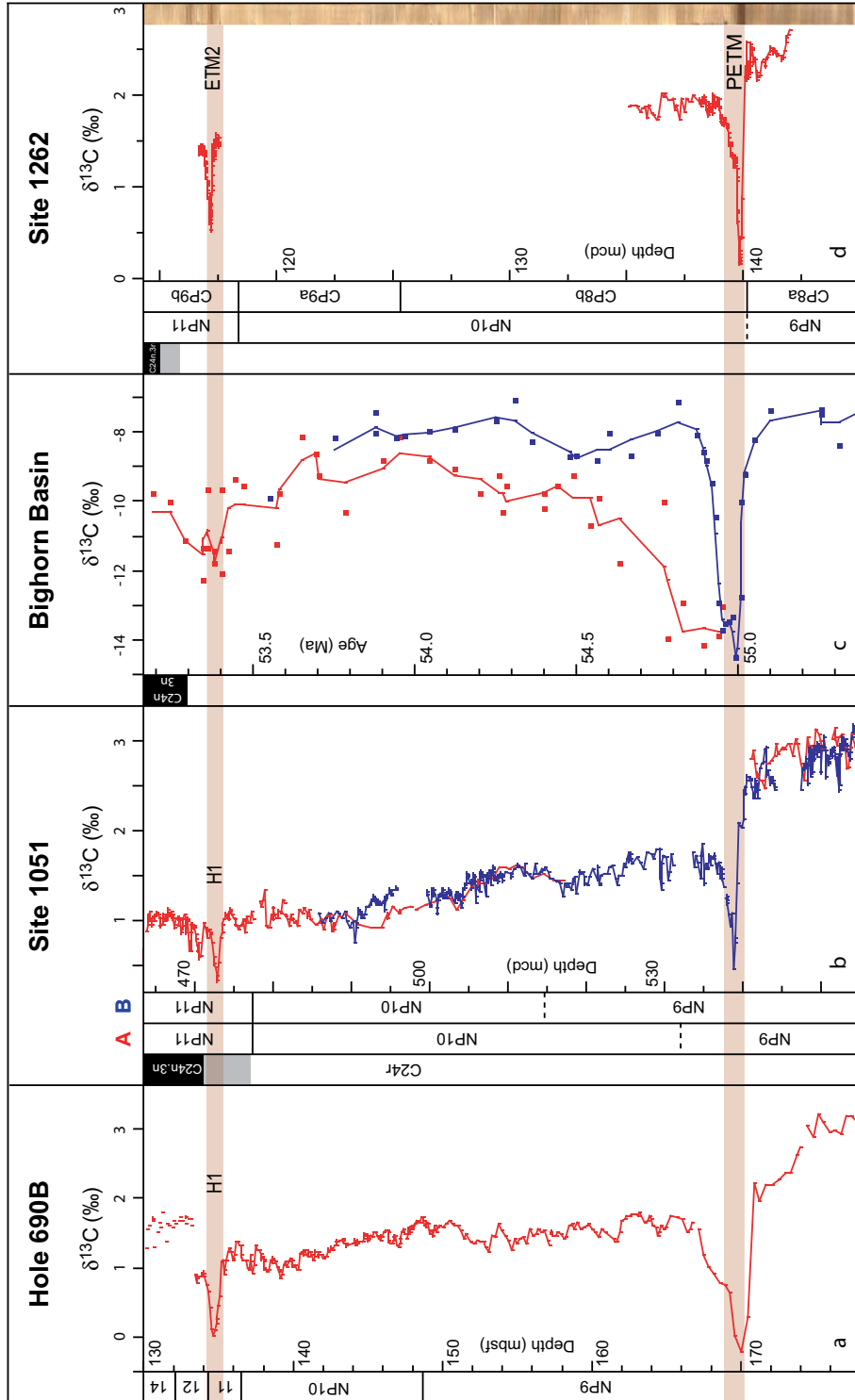
and La2004 (Laskar et al., 2004) orbital solutions using a Gaussian filter centred at a frequency of 0.0095 ± 0.002 per kyr (Appendix Fig. 3.5). Subsequently, the extracted short and long eccentricity related components of the L* and MS records from Site 1262 were tuned using the most likely combination of both the ~2.25Myr related amplitude changes in the ~100kyr cycle and ~405kyr cycle (Fig. 2.3).

Global significance of the ETM2 event (and *Elmo* horizon)

To illustrate the global significance of the ETM2 event we compared our high-resolution $\delta^{13}C_{bulk}$ records across the *Elmo* horizon (this study) and PETM (Chapter 1) of Site 1262 with those obtained from the subtropical Northwest Atlantic ODP Site 1051 and the high-latitude Southern Ocean ODP Site 690 (Cramer et al., 2003) (Appendix Fig. 3.6). These sites revealed a relatively strong negative excursion (termed H1) just below C24n/C24r (Site 1051) and within NP11 (Sites 690 and 1051), which bears strong resemblance with a similar negative excursion in the North Atlantic DSDP Site 550, and equatorial Pacific DSDP Site 577 (Cramer et al., 2003) (not shown). Given the good magnetobiostratigraphic constraints as well as the relative strength of this carbon isotope excursion with respect to that of the PETM, we conclude that the H1 is the equivalent of the ETM2 event. It should be noted that of all these sites only the magnetobiostratigraphy of Site 690 seems questionable, probably due to a series of unconformities immediately above the transient event H1 as indicated by the tight succession of the NP10/NP11, NP11/NP12, and NP12/NP14 zonal boundaries (Aubry et al., 1996; Ali et al., 2000).

To further illustrate that the CIE associated with the ETM2 is not only recorded in the marine realm, we also plotted the paleosol soil nodule carbonate isotope record from the Bighorn Basin (Koch et al., 2003) in Appendix Fig. 3.6. Although this record seems to reflect a noisy signal in some parts, the application of a 3 point moving average clearly demonstrate that the long-term Eocene $\delta^{13}C$ low is superimposed by two excursions: one definitely related to the PETM and the other less amplified excursion in the interval just below the C24n/r boundary to, most likely, the ETM2 event.

174

Appendix 4

Supporting Chapter 3 of this thesis on the PETM of the Arctic Ocean, this appendix contains three figures, additional references, information on stratigraphic issues and an extended description of the TEX_{86}' proxy. Further, it is discussed in detail why our records are not influenced by preservation, and additional evidence for bottom water anoxia during the PETM is presented.

Relative stratigraphic position of Core 31X

The stratigraphic position of the 55 cm recovered section of Core 302-4A-31X relative to Cores 30X and 32X is uncertain (Chapter 3, Fig. 2). It may be located anywhere in the interval between 384.54 and 388 meters composite depth (mcd). For illustration purposes, this core was placed 1m lower than indicated in Backman et al. 2006).

Description and calibration of TEX$_{86}$'

Originally TEX$_{86}$ values were calculated as described in Schouten et al. (2002) and converted to sea surface temperature (SST). However, the glycerol dialkyl glycerol tetraether (GDGT) lipid containing three cyclopentane rings (GDGT-3), almost always the least abundant GDGT lipid in marine sediments, was unusually high in Core 302-4A-32X (Appendix Fig. 4.2A). Since terrestrial organic matter also contains isoprenoid GDGT lipids with cyclopentane rings (Weijers et al., 2004; Weijers, J Schouten, S., Sinninghe Damsté, J.S., unpublished results), it is likely that the high terrestrial input in this section has disturbed the aquatic signal. The high abundance of GDGT-3 resulted in unusually high TEX$_{86}$ values in Core 32X. To circumvent this problem, TEX$_{86}$' was devised which has the same definition as TEX$_{86}$ except that isomer GDGT-3 was removed from the denominator (Schouten et al., 2002). The TEX$_{86}$' was determined for 104 marine surface sediments and found to correlate very well with annual mean SST: TEX$_{86}$' = 0.016 x SST + 0.20 with R^2 = 0.93 (Appendix Fig. 4.2B). This equation was used to convert TEX'$_{86}$ into SST. Sediments from Cores 30X and 31X show a normal marine tetraether lipid distribution, i.e., showing a very minor peak at GDGT-3, resulting in the TEX$_{86}$' values only slightly different from TEX$_{86}$ values (Appendix Fig. 4.2C). Interestingly, the top part of Core 30X, which shows a large terrestrial influence (Fig. 2), shows again a relatively large offset between TEX$_{86}$' and TEX$_{86}$, evidencing a larger contribution of the GDGT-3. This is consistent with a terrestrially-derived contribution to the GDGT-3 peak.

Which temperature does TEX$_{86}$' indicate in the Arctic Ocean?

TEX$_{86}$ and TEX$_{86}$' are calibrated by core top analysis to mean annual mean SST. This empirical relation is not the same as a causal relationship. Several studies have shown that the cell number of crenarchaeota in the water column strongly depends on the season (Murray et al., 1999). In most studies a negative correlation has been observed between the cell abundance of crenarchaeota and phytoplankton, likely because they compete for the nutrient ammonia. As crenarchaeota are chemoautotrophic organisms (Wuchter et al., 2003) and thus not directly depend on light it is likely that crenarchaeota predominantly thrived during times of low cell abundances of phytoplankton and low light intensities, i.e. in the Arctic winter. However, for the crenarchaeotal signal to reach the sediment

floor a significant sedimentation flux is needed. In the present day ocean significant organic carbon fluxes are observed during periods of high phytoplanktonic productivity because an active food web leads to grazing and feacal pellet packaging (Wakeham and Canuel, 1988; Wakeham and Lee, 1993). In agreement with this we recently recorded the highest fluxes of crenarchaeotal lipids in the Arabian Sea coinciding with the periods of high productivity, despite that their relative abundance was lower in these periods (Wuchter C., Schouten S., Wakeham,
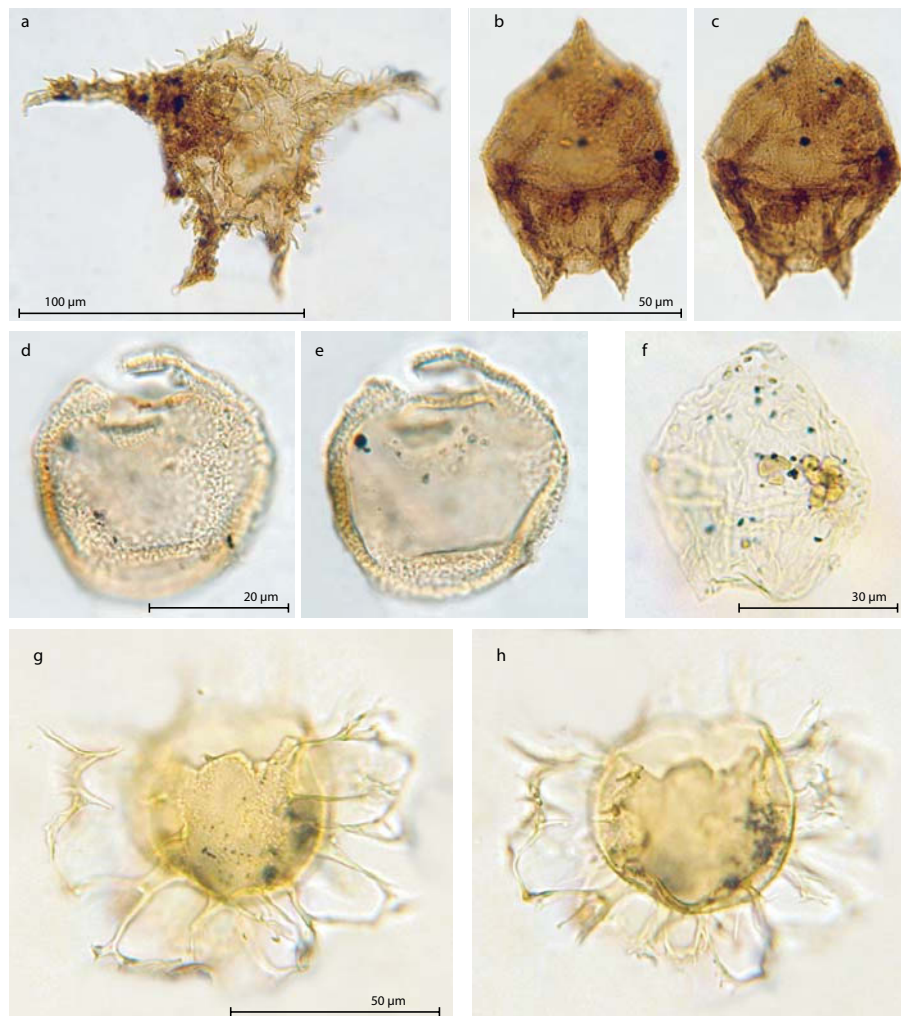
Appendix Figure 4.1 Light microscope photos of dominant dinocyst taxa across the PETM of IODP Hole 302-4A. **a.** *Apectodinium augustum* (302-4A-30X, 101-103 cm; Slide 1, England Finder Coordinates S32-1); **b, c.** *Cerodinium wardenense* (302-4A-30X-3, 81-83 cm; Slide 1, F37-0); **d, e.** *Membranosphaera* spp. (302-4A-30X-1, 141-143 cm; Slide 1, L31-3); **f.** *Senegalinium* spp. (302-4A-30X-3, 101-103 cm; Slide 1, L37-3); **g, h.** *Glaphyrocysta* spp. (302-4A-30X-1, 141-143 cm; Slide 1, J43-4).

S.G. and Sinninghe Damsté, J.S., unpublished results). In the Eocene Arctic Ocean the bulk of the signal will be derived from those periods with highest biological productivity, which at this high latitude must be the summer months. Hence we refined our interpretation of the TEX_{86}' estimates by suggesting that its signal in the Eocene Arctic Ocean, although calibrated to globally-derived annual mean SSTs, may record the, on average, higher summer SSTs due to the flux-dependency of the signal.

Preservation of the organic matter used in this study

Water column anoxia, in this paper indicated by the laminated sediments and the presense of isoreneratene derivatives, will lead to an improved preservation of certain organic compounds (Sinninghe Damsté et al., 2002). Below, we discuss the preservation of the different types of organic matter used in this paper and conclude that selective preservation did not affect our proxy records.

The presence of isorenieratene derivatives has been frequently used to detect anoxia extending up into the photic zone of the water column during the Phanerozoic (Koopmans et al., 1996; Sinninghe Damsté and Koster, 1998), including late Pliocene sapropel formation in the eastern Mediterranean (Passier et al., 1999). These compounds are derived from photosynthetic green sulfur bacteria which require both light and free sulfide (i.e., euxinic conditions) to thrive. In the particular, these organisms are found in lakes and marine settings where the water column is euxinic such as the present day Black Sea (Sinninghe Damsté et al., 1993). Accordingly, the presence of isorenieratene derivatives in ACEX Cores 30X and 31X indicates that euxinic conditions prevailed in the photic zone in the Arctic ocean during the PETM. These compounds preserve quite well, even when the water column is re-oxygenated and sediments are inhabited by benthic organisms (Kenig et al., 2004). Therefore we exclude selective preservation as possible bias on the presence/absence pattern of these compounds. Moreover, well preserved palynomorphs and substantial organic matter concentrations (~2% TOC) outside the laminated interval with isorenieratene derivatives, indicates that no severe organic matter degradation occurred. In this respect, we also exclude a bias on the terrestrial vs. marine palynomorph ratio, since it has recently been shown that preferential preservation of terrestrial palynomorphs only occurs in well-oxygenated bottom water settings (Reichart and Brinkhuis, 2003).

The terrestrial and marine compounds used in the BIT index represent structurally very similar compounds (Hopmans et al., 2004). It has been shown that the relative distribution of the different isomers of glycerol dialkyl glycerol tetraethers (GDGTs) is independent of the oxygen concentration in the water column (Schouten et al., 2004). Thus, the absolute amounts of GDGTs may have increased

within the laminated interval, but their relative distribution, i.e. the BIT index, has remained unaffected.

Bottom water anoxia at the PETM

Organic linings of benthic foraminifera are common through the latest Palaeocene and earliest Eocene except during the photic zone euxinia, indicated by isorenieratane (Appendix Fig. 4.3A). Sediments from the latter interval are laminated (Appendix Fig. 4.3B), which implies that no bioturbation occurred after deposition of the sediments and that bottom waters were anoxic. Despite a large scatter % TOC is on average ~1.3% higher during the PETM compared to the latest Palaeocene. Unfortunately, due to the core recovery problems and potential changes in siliciclastic sediment supply related to the transgression there is relatively poor grip on sediment accumulation rates across the studied interval. However, some of the enhanced % TOC may be due to increased nutrient supply by rivers, resulting in higher phytoplankton production and, under anoxic bottom water conditions, high organic matter accumulation.
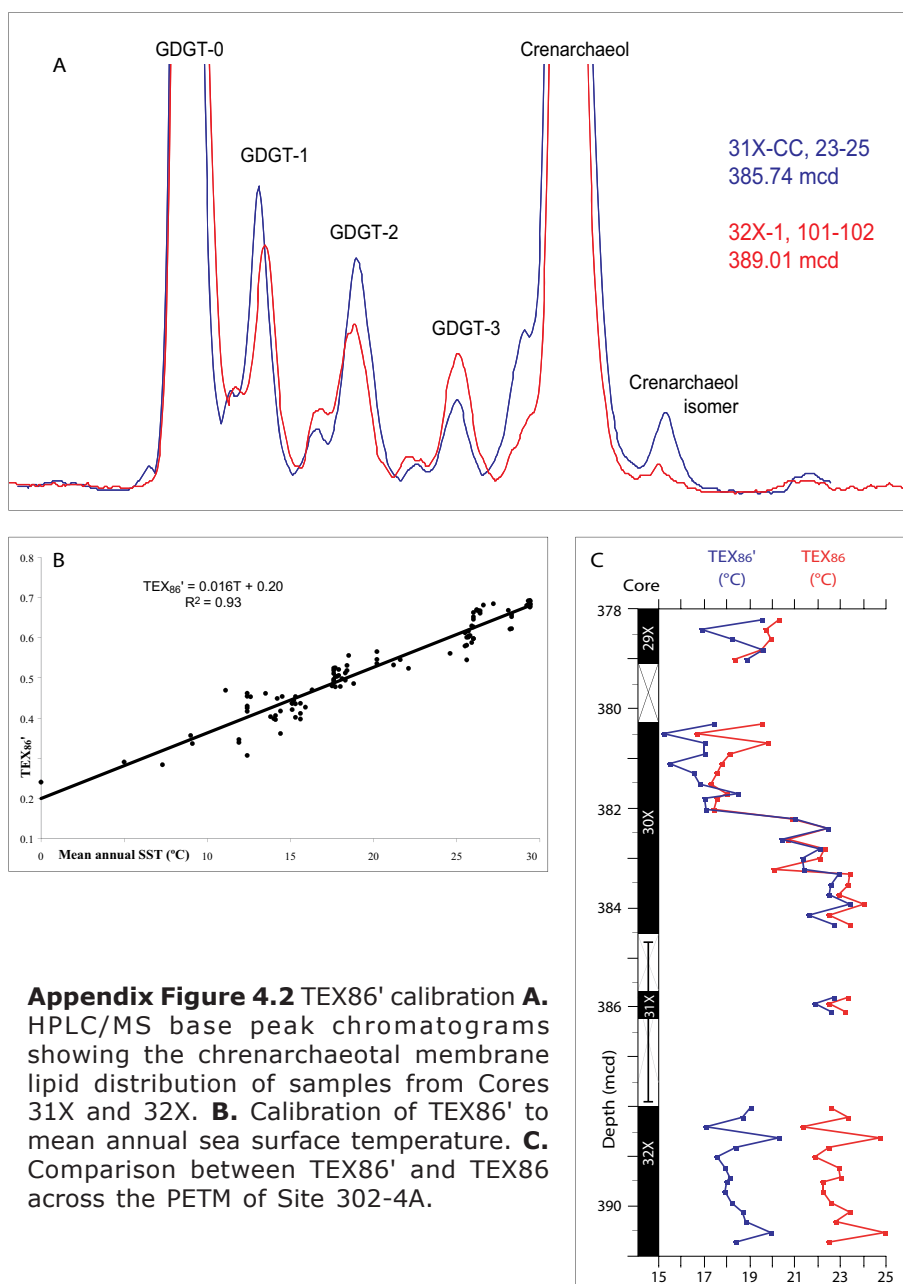
Appendix Figure 4.2 TEX86' calibration **A.** HPLC/MS base peak chromatograms showing the chrenarchaeotal membrane lipid distribution of samples from Cores 31X and 32X. **B.** Calibration of TEX86' to mean annual sea surface temperature. **C.** Comparison between TEX86' and TEX86 across the PETM of Site 302-4A.

Appendix Figure 4.3 (right) Additional indicators for water column euxinia and terrestrial influence. **A.** Isorenieratane and foraminifer lining distribution through the latest Palaeocene - earliest Eocene. Laminated interval indicated by stripes. Laminae are unclear in Core 31X due to drilling disturbance. The hydrogen index shows a substantial increase during the PETM, consistent with increased aquatic versus terrestrial organic matter. Despite significant scatter, average % Total Organic Carbon (TOC) increases by ~1% at the PETM. **B.** Core picture (interval 302-4A-30X-3, 123-129 cm) showing laminations.
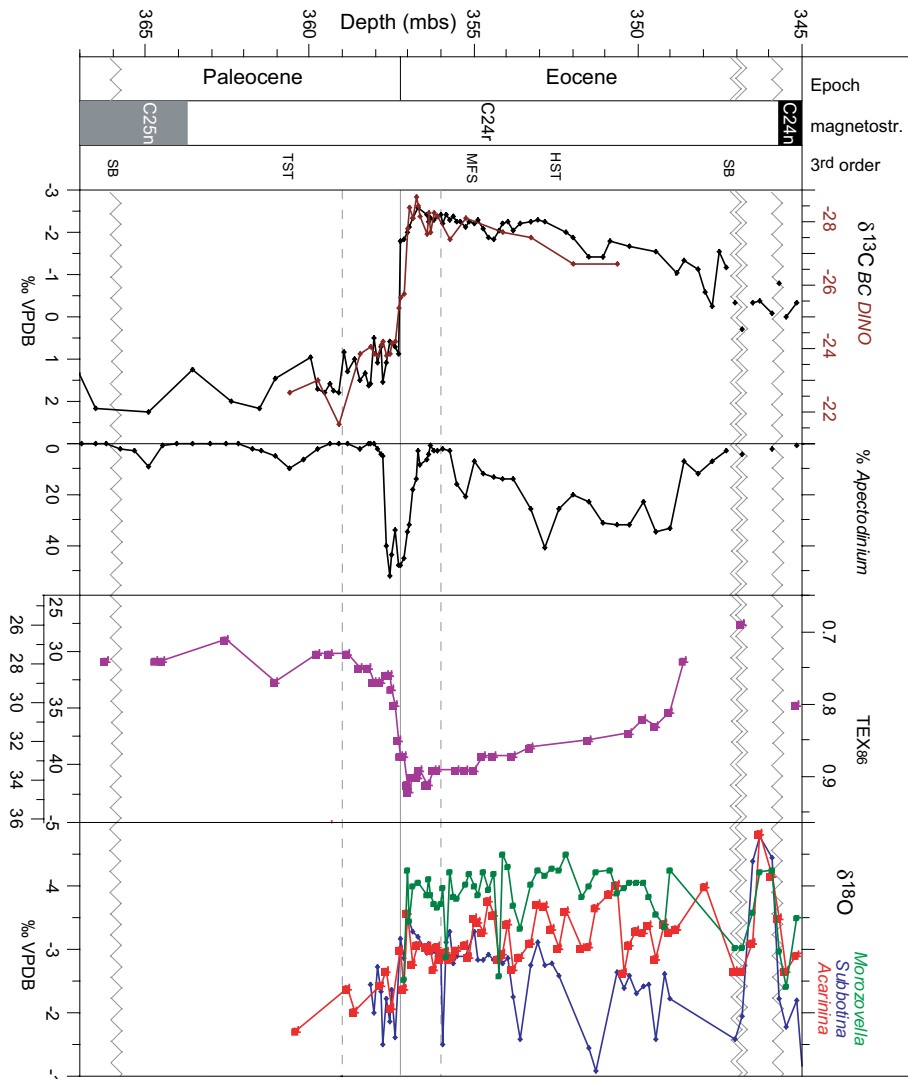
180
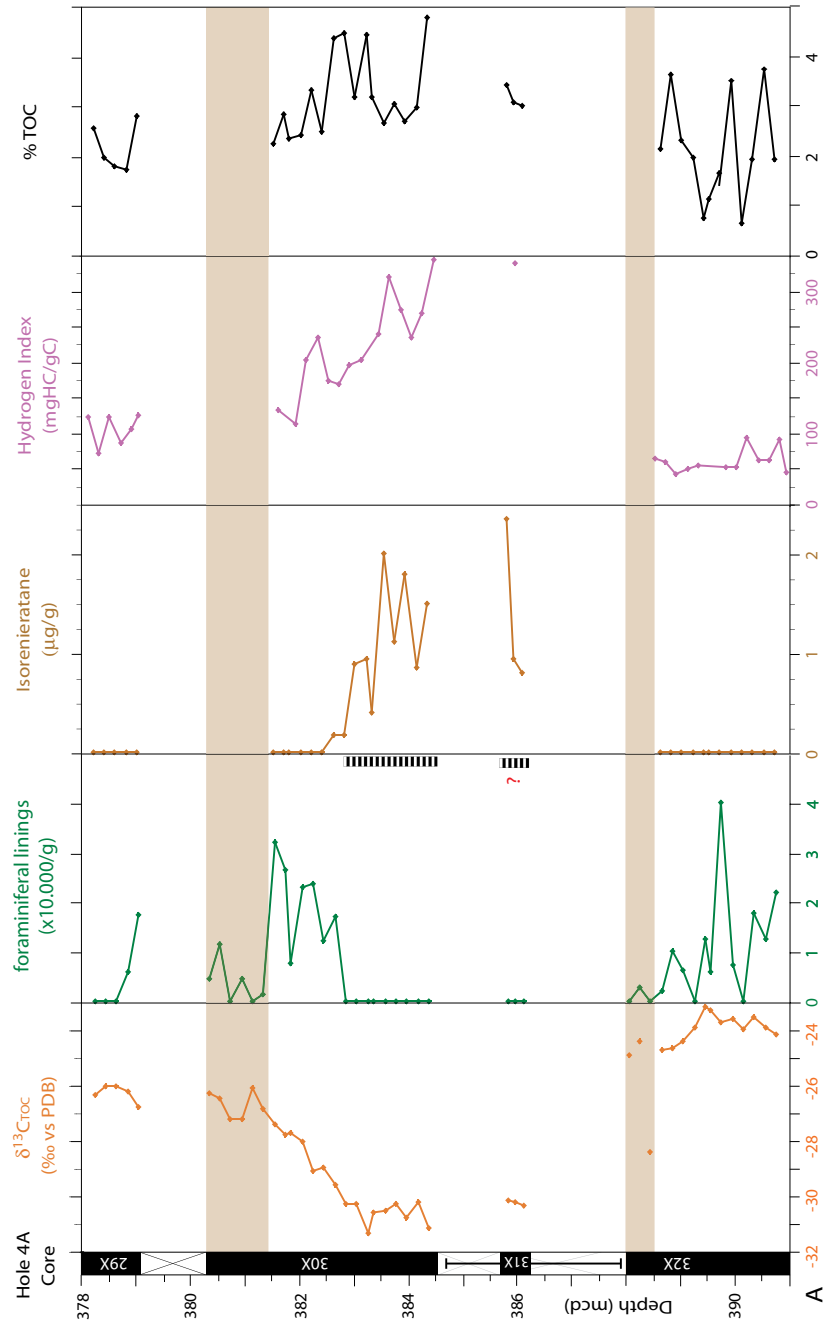
Appendix 5

Supporting Chapter 7 of this thesis, which reports on the onset of the *Apectodinium* acme and global warming before the carbon isotope excursion, this appendix contains three figures, additional references, and extended description of the methods. Further, potential precession forcing on the dinocyst records at Bass River is discussed.

Appendix Figure 5.1 High-resolution records across the PETM at Bass River, New Jersey. BC = bulk carbonate, DINO = dinocysts, VPDB = Vienna Pee Dee Belimnite, mbs = meters below surface. Scales at TEX$_{86}$ represent temperatures calibrations by Schouten et al. (2002) for the top bar and by Schouten et al. (2003) for the lower bar. Stable isotope data on carbonate are from John et al. (John et al., in prep).
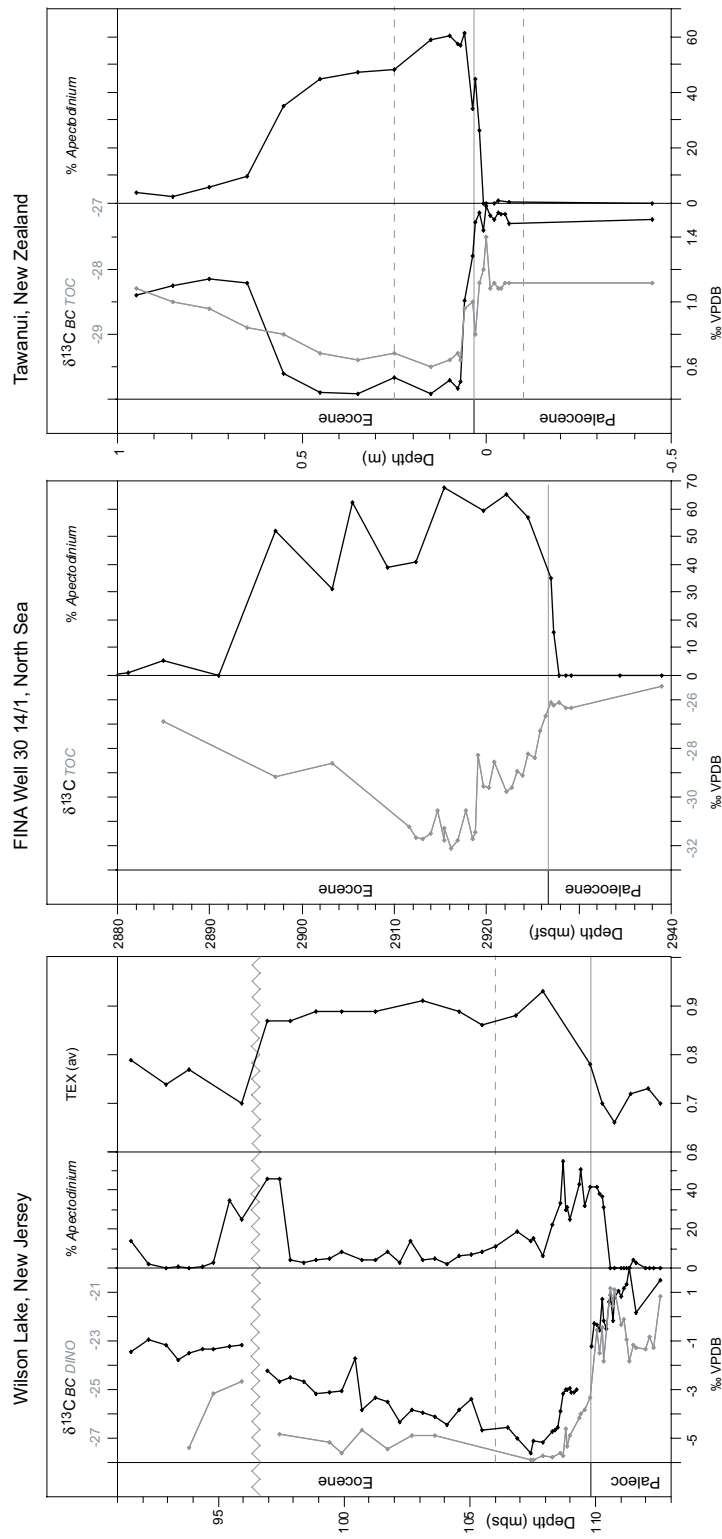
Appendix Figure 5.2 High-resolution records across the PETM at Wilson Lake, New Jersey (bulk carbonate stable isotope data from Chapter 4), FINA Well 30 14/1, North Sea and Tawanui, New Zealand (data from Crouch et al., 2001). BC = bulk carbonate, DINO = dinocysts, VPDB = Vienna Pee Dee Belimnite, mbs = meters below surface.

Methods

Palynology

Palynological processing was performed using standard methods (c.f., Sluijs et al., 2003). In short, samples were freeze dried and to ~10g of material a known amount of *Lycopodium* spores were added. Then, the sample was treated with 30% HCl and twice with 38% (HF) for carbonate and silicate removal, respectively. Residues were sieved using a 15-μm nylon mesh sieve to remove small particles. Samples from the North Sea were sieved in a 15-μm steel mesh sieve and subsequently oxidized for 20 minutes in Schultz Reagens at 80°C to reduce the amount of amorphous organic matter, and sieved again over a 15-μm nylon mesh sieve. To break up clumps of residue, the sample was placed in an ultrasonic bath for a maximum of 5 min, sieved again, and subsequently concentrated to 1 ml, of which 7.5-10 μl was mounted on microscope slides. Slides were counted up to a minimum of 200 dinocysts. Absolute quantitative numbers were calculated using the relative number of palynomorphs per counted *Lycopodium* spores.

TEX$_{86}$ analyses

For the TEX$_{86}$ analyses, powdered and freeze-dried sediments (20 g dry mass) were extracted with a Dionex Accelerated Solvent Extractor using a 9:1 mixture of dicholormethane (DCM) and methanol (MeOH). The extract was fractionated into apolar and polar fractions, containing the crenarchaeotal lipids using a small column with activated alumina and using hexane/DCM (9:1;v/v) and DCM/MeOH (1:1;v/v) as eluents, respectively. Polar fractions were dissolved in hexane/propanol (99:1;v/v), and filtered through 0.45 μm PTFE filters. The samples were analyzed with an Thermo Finnigan Quantum Ultra (San Diego, CA, USA) triple quadrupole LC-MS and separation was performed on an Econosphere NH2 column (4.6 × 250 mm, 5 μm; Alltech, Derfield, IL, USA), maintained at 30°C. The GDGTs were eluted using a changing mixture of (A) hexane and (B) propanol as follows, 99 A:1 B for 5 min, then a linear gradient to 1.8 B in 45 min. Detection was achieved using atmospheric pressure chemical ionization-mass spectrometry of the eluent. Single Ion Monitoring (SIM) was set to scan the 5 [M+]+H ions of the GDGTs with a dwell time of 237 ms for each ion. All TEX$_{86}$ analyses were performed at least in duplicate. Also the concentration of branched and isoprenoid tetraether lipids (BIT index, Hopmans et al., 2004) was measured to constrain the concentration of terrestrially derived GDGTs. This concentration was very low throughout the section (Chapter 6).
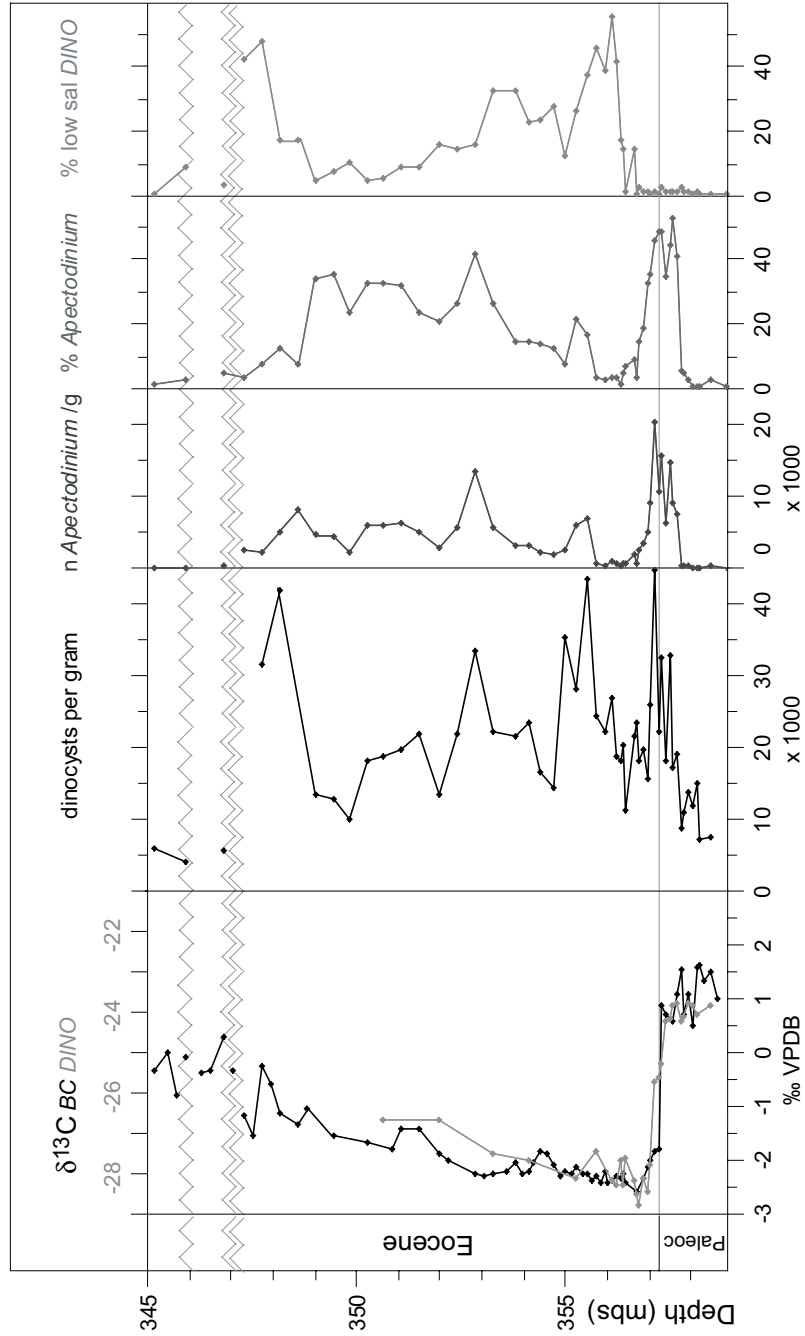
Appendix Figure 5.3 High-resolution dinocyst records across the PETM at Bass River (bulk carbonate stable isotope data from John et al., in prep). BC = bulk carbonate, DINO = dinocysts, VPDB = Vienna Pee Dee Belimnite, mbs = meters below surface.

Organic $\delta^{13}C$ measurements

For the $\delta^{13}C_{DINO}$ records, the 40-125 µm size fraction of the palynological residues, which are nearly barren of organic particles other than dinocysts, were isolated using nylon mesh sieves, and oven-dried. For the $\delta^{13}C_{TOC}$ analyses, samples were freeze dried and powdered. The $\delta^{13}C$ analyses were done with a Fison NA 1500 CNS analyzer, connected to a Finnigan Delta Plus mass spectrometer. Analytical precision determined by replicate analyses was better than 0.1‰.

Precession forcing on *Apectodinium* abundance at Bass River

Estimates for the duration of the CIE range between 130 kyr and 220 kyr (Röhl et al., 2000; Farley and Eltgroth, 2003) but likely close to 170 kyr (Röhl et al., in prep). Given this, sedimentation rates through the 10.3 meter thick CIE at Bass River are ~6.1 cm.kyr⁻¹. However, the upper bound of the CIE is a sequence boundary (Chapter 6), which implies that the upper part of the CIE is not represented in this section. This inhabits estimation of the portion of the CIE represented in our records, as well as sedimentation rates. However, we hypothesize that the 5 or 6 cyclic fluctuations in the relative and absolute abundance records of *Apectodinium* and the number of dinocysts per gram of sediment could be related to precession forcing (Appendix Fig. 5.3). Ecologically, this would imply that neritic surface water parameters, such as salinity, nutrient levels and stratification varied as a result of precession forcing, which has been recorded many times in dinocyst records from neritic Eocene deposits (e.g., Röhl et al., 2004b). Five cycles are present in the record, but considering the lower one is associated with transgressive systems tract and thus likely with lower sedimentation rates (Appendix Fig. 5.3) this may actually represent two precession cycles. However, the lower one of these two predates the CIE, so 5 cycles are present within the CIE. Five cycles would imply that ~105 kyr of PETM section is present at Bass River. Resulting sedimentation rates of ~10 cm.kyr⁻¹ on average within the PETM.